Geochemistry Geophysics Geosystems G3
AN ELECTRONIC JOURNAL OF THE EARTH SCIENCES
Published by AGU and the Geochemical Society

Article
Volume 7, Number 11
3 November 2006
Q11002, doi:10.1029/2006GC001378
ISSN: 1525-2027

Detecting compaction disequilibrium with anisotropy of magnetic susceptibility

Kurt Schwehr
Scripps Institution of Oceanography, La Jolla, California 92093-0220, USA

Now at Center for Coastal and Ocean Mapping, Chase Ocean Engineering Laboratory, 24 Colovos Road, Durham, New Hampshire 03824, USA (kurt@ccom.unh.edu)

Lisa Tauxe and Neal Driscoll
Scripps Institution of Oceanography, University of California, San Diego, La Jolla, California 92093-0220, USA (ltauxe@ucsd.edu; ndriscoll@ucsd.edu)

Homa Lee
U.S. Geological Survey, MS 937, 345 Middlefield Road, Menlo Park, California 94025-3561, USA (hjlee@usgs.gov)

[1] In clay-rich sediment, microstructures and macrostructures influence how sediments deform when under stress. When lithology is fairly constant, anisotropy of magnetic susceptibility (AMS) can be a simple technique for measuring the relative consolidation state of sediment, which reflects the sediment burial history. AMS can reveal areas of high water content and apparent overconsolidation associated with unconformities where sediment overburden has been removed. Many other methods for testing consolidation and water content are destructive and invasive, whereas AMS provides a nondestructive means to focus on areas for additional geotechnical study. In zones where the magnetic minerals are undergoing diagenesis, AMS should not be used for detecting compaction state. By utilizing AMS in the Santa Barbara Basin, we were able to identify one clear unconformity and eight zones of high water content in three cores. With the addition of susceptibility, anhysteretic remanent magnetization, and isothermal remanent magnetization rock magnetic techniques, we excluded 3 out of 11 zones from being compaction disequilibria. The AMS signals for these three zones are the result of diagenesis, coring deformation, and burrows. In addition, using AMS eigenvectors, we are able to accurately show the direction of maximum compression for the accumulation zone of the Gaviota Slide.

Components: 9895 words, 12 figures, 3 tables.

Keywords: anisotropy of magnetic susceptibility; submarine landslides; slope failure; apparent overconsolidation.

Index Terms: 1518 Geomagnetism and Paleomagnetism: Magnetic fabrics and anisotropy; 3002 Marine Geology and Geophysics: Continental shelf and slope processes (4219); 3070 Marine Geology and Geophysics: Submarine landslides.

Received 2 June 2006; **Revised** 23 June 2006; **Accepted** 29 August 2006; **Published** 3 November 2006.

Schwehr, K., L. Tauxe, N. Driscoll, and H. Lee (2006), Detecting compaction disequilibrium with anisotropy of magnetic susceptibility, *Geochem. Geophys. Geosyst.*, *7*, Q11002, doi:10.1029/2006GC001378.

1. Introduction

[2] Understanding and predicting when and where submarine landslides will occur is a still a challenge to the marine science community [e.g., *Kayen et al.*, 1989; *Schlee and Robb*, 1991; *Booth et al.*, 1993; *Locat and Lee*, 2002]. It is imperative to develop adequate techniques that allow insight into the prefailure and post-failure stratigraphy.

[3] Slope failure and creep may sometimes be imaged with multibeam and chirp data [e.g., *Edwards et al.*, 1995; *O'Leary and Laine*, 1996; *Eichhubl et al.*, 2002; *Hill et al.*, 2004], but these techniques do not provide the full spectrum of information required to completely interpret these features. Layers with excess water create zones of weakness in the strata that may localize failure or slide surfaces [*Dugan and Flemings*, 2000], whereas unconformities may lead to apparent overconsolidation that record the past history of failures and erosion. *Mello and Karner* [1996] describe deviations from normal consolidation as compaction disequilibria. While many methods for exploring compaction disequilibria are destructive [*Lambe and Whitman*, 1969], anisotropy of magnetic susceptibility (AMS), the focus of this study, provides a minimally-invasive approach to quickly assess core sediments.

[4] The ability to detect the two types of compaction disequilibria (underconsolidation and apparent overconsolidation) is another step in predicting the recurrence interval and size of submarine landslides that helps determine the tsunamigenic potential of an area [*Driscoll et al.*, 2000; *Ward*, 2001]. Continental shelf and slope areas are becoming increasingly important for economic development of hydrocarbons, wave energy, and other resources. Slope stability is a critical engineering component to managing safe development.

[5] In this paper, we will first discuss the types and causes of compaction disequilibria including high water zones that are underconsolidated and apparent overconsolidated zones associated with exhumation by landslides. We will then describe how AMS can be used to identify compaction disequilibria. Finally, we will apply AMS techniques to the Santa Barbara Basin margin, a region with known slope instabilities [e.g., *Fisher et al.*, 2005].

2. Compaction Disequilibria

2.1. Underconsolidation

[6] Bulk permeability of sediment is determined by a combination of local microstructure, grain permeability and the degree of macroscale permeability determined by material continuity. In Figure 1a, we show a schematic drawing of sediment undergoing consolidation. Clay particles tend to have positively charged edges and negatively charged faces. These electrostatic forces tend to cause clay particles to aggregate edge to face (EF) [*Bennett et al.*, 1991] as shown in the upper part of Figure 1. During consolidation, volume loss results in the collapse of the clay structure to the more compact face to face (FF) structure.

[7] Overpressured zones are likely to occur in areas with high rates of sedimentation because the rate of pore fluid escape cannot keep pace with the accumulating overburden [*Mello and Karner*, 1996]. Differences in permeability associated with small changes in consolidation, mineralogy, and bioturbation may retard upward migration of fluids. Zones of excess water content can develop below such layers. These high water content zones could inhibit the normal consolidation of the clay depositional structure, thus keeping the EF clay contacts from changing into FF contacts (Figure 1a). Under load, these open structures collapse to a stable book structure that cannot reinflate. This inability to reinflate with increasing pore pressure implies that undercompacted horizons are primary depositional features created as the overlying layer is deposited.

2.2. Apparent Overconsolidation

[8] Overconsolidation is a reduction in the water content producing an apparent disequilibrium, where material is more consolidated than predicted for a given depth according to empirical compaction-loading curves. One factor leading to apparent overconsolidation is the existence of erosional unconformities. First, sediments are deposited and buried in an unperturbed compaction scenario. If overlying sediments are removed by slope failure or erosion, and the underlying material has undergone some component of inelastic deformation (as is the case for clays), then that inelastic strain will remain, resulting in an apparently overconsolidated zone.

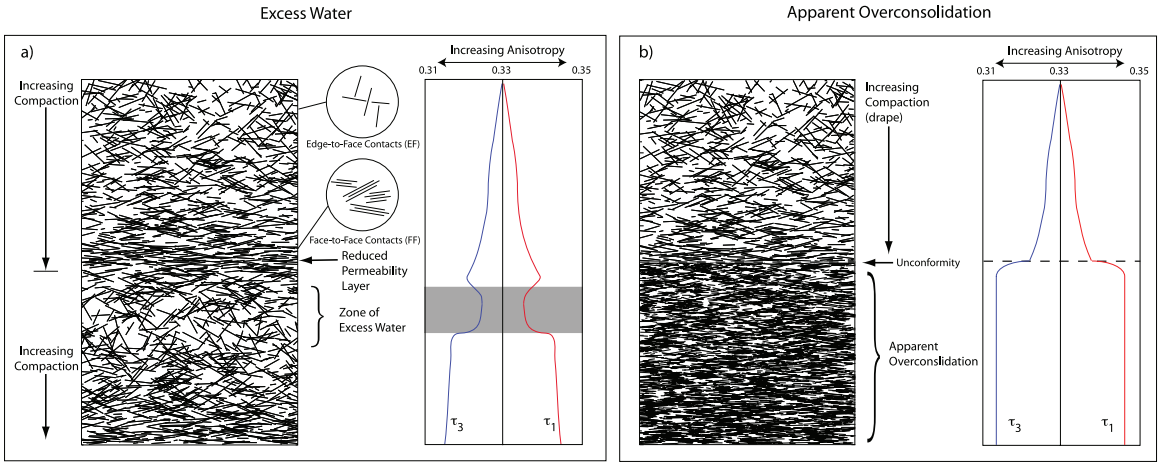

Figure 1. Schematic of compaction disequilibriums. (a) Clay particles in sediment undergoing compaction. Particles compact and create a reduced permeability layer. Below this layer, excess water content can in turn retard compaction. The excess is generated by the low-permeability layer that temporarily reduces upward migration of pore fluids. Below the zone of excess water, compaction increases down section. The graph on the right is an idealized model of how compaction affects the anisotropy of magnetic susceptibility (AMS) fabric. As compaction progresses, overall anisotropy increases. Zones of excess water are detected by regions of reduced anisotropy (marked with a gray band). (b) Platy clay particles in sediment undergoing compaction with a zone of apparent overconsolidation created by an unconformity.

[9] Shock induced dewatering can also cause overconsolidation [*Lee et al.*, 2004]. *Locat and Lee* [2002] summarized work showing that with repeated shake events, sediments that do not fail may lose water, compact, and become stronger. They term such events ''seismic strengthening.''

3. Magnetic Fabrics

[10] AMS is a well-established technique for studying fabrics of geologic materials (summarized by *Tarling and Hrouda* [1993] and *Tauxe* [1998]). AMS of clay-rich sediments is believed to be dominated by paramagnetic shape anisotropy of the clay minerals and small magnetic particles that are generally attached to the clay fabric [*Kodama and Sun*, 1992]. When hemipelagic sediments are deposited in quiescent environments, elongate particles deposit with their long axes subparallel to the bedding plane. This mode of deposition produces weakly oblate to isotropic sediment fabrics.

[11] Detection of underconsolidation and unconformities is possible with nonmagnetic techniques. However, the AMS magnetic fabric method complements the other data types and, more importantly, helps identify compaction disequilibria features when they are difficult to detect by other approaches. Other magnetic fabric methods include anisotropy of isothermal remanent magnetization (AIRM) and anisotropy of anhysteretic remanent magnetization (AARM) [*McCabe et al.*, 1985]. Unlike AIRM and AARM, AMS is magnetically nondestructive (it does not affect the magnetic remanence) and is the fastest of the magnetic techniques to apply. AIRM and AARM both would yield additional insight into sediment deposition and deformation mechanisms, but are more time consuming to acquire. Moreover, AMS is strongly affected by the clay fabric, whereas remanent anisotropies are not directly sensitive to the clays and it is the clay fabric that is of concern here.

[12] Because AMS is sensitive to the compaction state of clay-rich sediments [e.g., *Housen et al.*, 1996; *Kopf and Berhman*, 1997; *Kawamura and Ogawa*, 2004], it is a promising tool for exploring regions of rapid sediment loading. Accelerated deposition and sediment loading tend to lead to a higher occurrence of slope failures, because rapid sedimentation usually is associated with higher water content [*Schwab et al.*, 1993]. The majority of compaction and dewatering occurs typically from the sediment-water interface down through the top tens of meters of sediments, with the majority being completed by depths of around 150 meters [*Kawamura and Ogawa*, 2004]. When loaded, clay sediments compact and compaction signatures can be observed with AMS measurements as an increasing oblate anisotropy with the

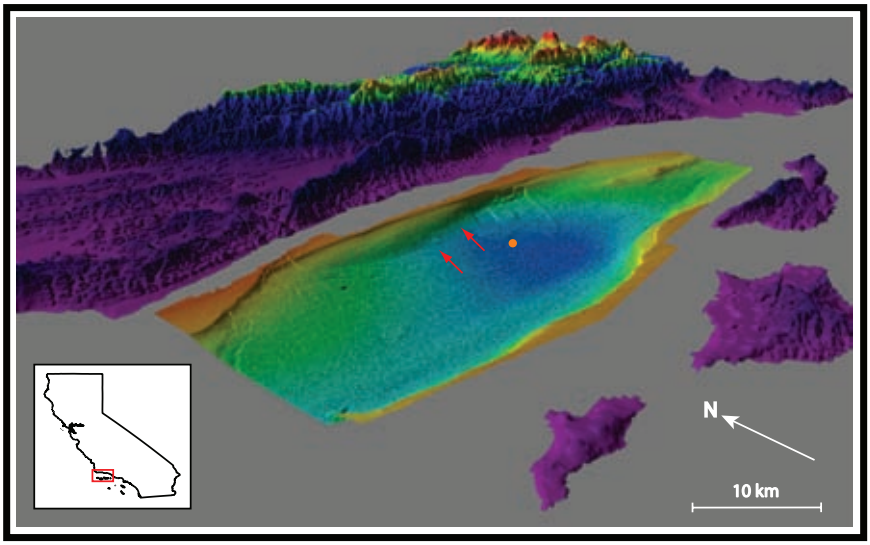

Figure 2. The Santa Barbara Basin (red box in the inset) is a part of the California Borderlands and is located south of the Transverse Ranges in California. The motion on the San Andreas Fault System has created a closed basin that is partially shielded from the flushing action of the California Current. Rapid deposition on steep slopes combined with frequent large earthquakes has resulted in a number of slides in the recent Holocene sediments. The study areas are marked with red arrows: the Gaviota slide on the left and the slope crack on the right. The bathymetry is from the MBARI EM300 multibeam survey [*Eichhubl et al.*, 2002]. Also shown is the location of ODP Site 893 (orange circle).

V_3 direction (eigenvector associated with the minimum eigenvalue using the terminology of *Tauxe* [1998] being near vertical. At depth, processes such as cementation and diagenesis begin to lock in the shape that is present and all of the "easy" compaction has been accomplished.

[13] For deep-sea sediments, *Kawamura and Ogawa* [2004] found that the compaction process progresses in either a gradual manner, or a stepwise function. *Kawamura and Ogawa* [2004] suggest that low permeability in overlying layers that retard dewatering may lead to regions of excess pore pressure as evidenced by large void ratios. In rapidly depositing sediments, the degree of compaction should allow AMS to detect these underconsolidation zones.

[14] According to *Kawamura and Ogawa* [2004], sedimentation rates have an influence on compaction, where water content remains higher to greater depths for faster sedimentation rates. The deep ocean cores used by *Kawamura and Ogawa* [2004] have sedimentation rates of 1.7 to 3.3 mm/kyr. Slow sedimentation rates allow pore fluids more time to diffuse through low-permeability layers. The conditions of faster rates found along continental margins preserve disequilibria to greater depths because there is less time for fluids to be expelled from the sediment column.

[15] The AMS signature for apparent overconsolidation would be an abrupt increase in the degree of anisotropy of the fabric. The AMS signature predicted for overconsolidation is illustrated in Figure 1b. The overall anisotropy is defined as the difference between the eigenvalues τ_i (which are scaled to sum to unity with the maximum being τ_1 and minimum being τ_3). Changes in the degree of anisotropy under normal consolidation would be a gradual increase in anisotropy as shown in the top of the core. An abrupt change to an FF fabric because of overconsolidation would be accompanied by an abrupt increase in the degree of anisotropy reflected by the increase in the separation of τ_1 and τ_3 (see Figure 1). Note that the relationship of τ_2 to the others (not shown) reflects the shape; where τ_2 is indistinguishable from τ_1, the shape is oblate. In contrast to overconsolidation, underconsolidation zones would be reflected by a decrease in degree of anisotropy as illustrated in Figure 1a.

[16] If AMS is able to detect these zones of overcompaction (compared to the expected sediment overburden and time), then it could provide a quick method to detect regions where the overlying sediment has been removed. To test the AMS

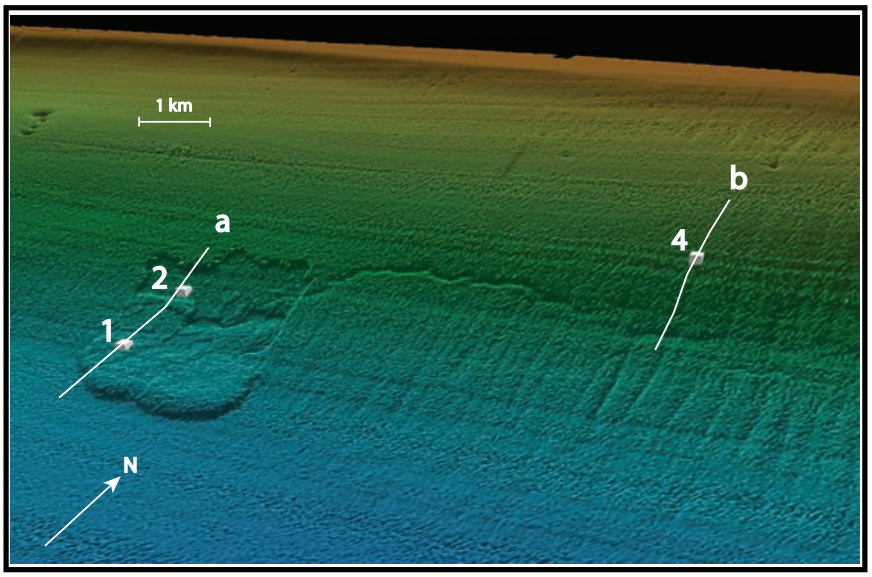

Figure 3. Enlargement of the Gaviota Slide on the northern slope of the Santa Barbara Basin shows a well-imaged underwater landslide. Two gravity cores were acquired within the slide boundaries; core 1 is in the accumulation zone (toe) of the slide. Core 2 is in the evacuation zone. A large crack on the right is connected to the Goleta Slide to the east. The crack extends east-west along the slope between the Gaviota and Goleta Slides for 8 km. It is between 5 and 20 m wide and appears to cut the many rills that run downslope. Core 4 is located 780 m upslope from the crack. The bathymetry is shown with a vertical exaggeration of 6x. CHIRP seismic lines a and b are shown in Figures 4 and 5, respectively.

method for detection of compaction disequilibria, we need a well-studied area with a high deposition rate and reasonably well-defined failure history. The Santa Barbara Basin and the Gaviota Slide provide such an environment.

4. Geologic Setting

[17] The Santa Barbara Basin (SBB) is located off the coast of Southern California (Figure 2) and is the northernmost basin in the California Borderland area. The basin is roughly 80 km by 32 km at its greatest extent. The northern end of the basin is blocked by the Santa Barbara coastline; the San Miguel, Santa Rosa, and Santa Cruz Islands delineate the southern extent of the basin. On the western side, the basin has a sill depth on the order of 460 m (located at approximately 120°28′27.06″W, 34.0°15′52.01″N) whereas on the eastern edge of the basin, the sill is shallower, being approximately 225 m. The maximum depth of the enclosed basin is 593 m (120°01′15.60″W, 34°12′19.44″N). The sills on the western and eastern boundaries inhibit the flushing of the bottom waters creating an anoxic basin. Typically, there are low oxygen concentrations starting at 470 m and the water column is depleted of oxygen by 570 m [*Edwards et al.*, 1995].

[18] The sediment accumulation rates in the SBB are extremely high and have been estimated to be on the order of 1400 mm/kyr [*Hendy and Kennett*, 2000]. The currents and sediment production in this particular region have been extensively studied [e.g., *Soutar and Crill*, 1977; *Reimers et al.*, 1990; *Bray et al.*, 1999; *Dorman and Winant*, 2000; *Oey et al.*, 2004; *Warrick et al.*, 2005]. During the winter months, sediment input is dominated by terrigenous input that corresponds to winter precipitation and erosion that occurs in California. At Ocean Drilling Project (ODP) site 893, the dominant terrigenous sources are the Santa Clara and Ventura Rivers [*Marsaglia et al.*, 1995; *Hein and Dowling*, 2001]. The northern slope area of the SBB is more likely to have the terrigenous sediment sourced from the Santa Ynez Mountains.

Table 1. Locations and Lengths of the Cores Collected on the R/V *Sproul* During August 2004[a]

Core	Latitude	Longitude	Depth, m	Length, m
1	34°21′40.2″	−120°06′28.8″	480	1.68
2	34°22′12.0″	−120°06′27.0″	439	0.73
4	34°22′44.4″	−120°03′25.8″	322	1.25
ODP 893	34°17′15.0″	−120°02′12.0″	577	187.00

[a] Ocean Drilling Project (ODP) Leg 146 Hole 893A is included as it is near the study area.

Spring months experience high biogenic productivity that is dominated by diatoms [*Thunell et al.*, 1995]. The productivity is probably driven by upwelling of nutrient-rich waters.

[19] The area around the SBB (Figure 2) is a tectonically active zone with frequent large earthquakes up to magnitude 7 [*Shaw and Suppe*, 1994]. The SBB has a large number of slope failure features, which could have been triggered by local earthquakes.

[20] The study area is the northern slope of the SBB bounded by the shelf break to the north, the basin floor to the south, the Goleta Slide to the east and the Conception Fan to the west. The Conception Fan appears to be inactive [*Fischer*, 1998].

[21] The swath bathymetry (Figure 3) was collected by the Monterey Bay Aquarium Research Institute (MBARI) using a 30 kHz EM300 multibeam system [*Eichhubl et al.*, 2002]. The soundings were gridded at 25 m cell spacing. The MBARI bathymetry gives an excellent view of the features in the basin that are on the scale of meters and larger (Figure 3).

4.1. Goleta

[22] The most prominent deformation feature observed in the SBB is the large Goleta Slide on the northeastern corner of the basin. The aerial distribution of this large feature is 11 by 14 km with three main areas of runout. The center runout has the highest topography, whereas the western runout has the lowest with a difference of about 50 m. The head scarps are located at the edge of the shelf-slope break and are steep with heights up to 50 m that transition into a number of blocks with large amounts of drape. The toes of the slides extend out into the basin 9–12 km, reaching to within 970 m of ODP site 893 (see Table 1 for location).

4.2. Gaviota

[23] The Gaviota Slide (Figure 3) is located to the west of the Goleta Slide and extends 3 km from the head scarp down to the bottom of the toe. The evacuation zone appears to have removed 6–8 meters of material (relief measured at the head scarp). The Gaviota Slide is a very recent feature as evidenced by the minimal pelagic drape mantling the slide scar. The slope break above the Gaviota head scarp is 100 meters below sea level (mbsl). The slope dips on average 3.6° down to the basin floor at 480 meters where the dip of the sea floor diminishes to about 0.5°. *Edwards et al.* [1995] estimated that the slide excavated 0.01–0.02 km^2 of sediment failing in two main stages. They report the details of the slide morphology and an event chronology.

[24] It is likely that the 21 December 1812 earthquake (estimated $M_w \approx 7.2$) triggered the Gaviota Slide [*Borrero et al.*, 2001]. *Borrero et al.* [2001] cite historical reports of a small tsunami observed along the coast just after the quake. *Edwards et al.* [1995] believe that the Gaviota Slide failed somewhere in the range of 1345 CE to 1871 CE with a best estimate of 1812 CE. The excavated scarp is covered by pelagic drape, which would constrain the age of the slide. However, these types of unconformities can be difficult to recognize in cores, especially after the horizons oxidize. Because of the contrast in the degree of compaction across the unconformity, it is possible that AMS fabric could be used to detect the unconformity.

4.3. Other Small Slides

[25] The main difference between the smaller slide structures in the basin compared to the Goleta Slide is that the smaller slides have much less runout. There are three areas, or groups, of small slides: the northeastern side of the basin, the very steep slides on the southern wall (not studied in this paper), and the Gaviota Slide on the northern side of the basin. There are undoubtedly a large number of smaller slides that are below the resolution of the EM300 multibeam system available at the time of the study.

[26] Two small slides on the northeastern corner of the basin lay between the Goleta Slide and the end of surface expression of the Mid-Channel trend anticline structure. These slides are on a shallow dipping slope and have well-defined head scarps. The slide just to the east of the Goleta has an evacuated zone at the top that is 0.6 km long with a slope of 1.4°, whereas the toe runs for 1.6 km on a slope of 1.2° with a maximum width of 0.97 km. The slide to the east has a double-humped slide scar and is difficult to see in the bathymetry. This structure has an overall slope of 1.4° and an total extent of 2.9 km from the headwall scarp to bottom of the toe.

[27] On the western edge of the basin is a very subtle slide centered at 120°18′37.80″W, 34°16′24.06″N described by [*Edwards et al.*, 1995]. The upper deformed section of the slide is 4 km long and dips an average of 0.9°, whereas the lower surface is smooth and extends about 2.4 km

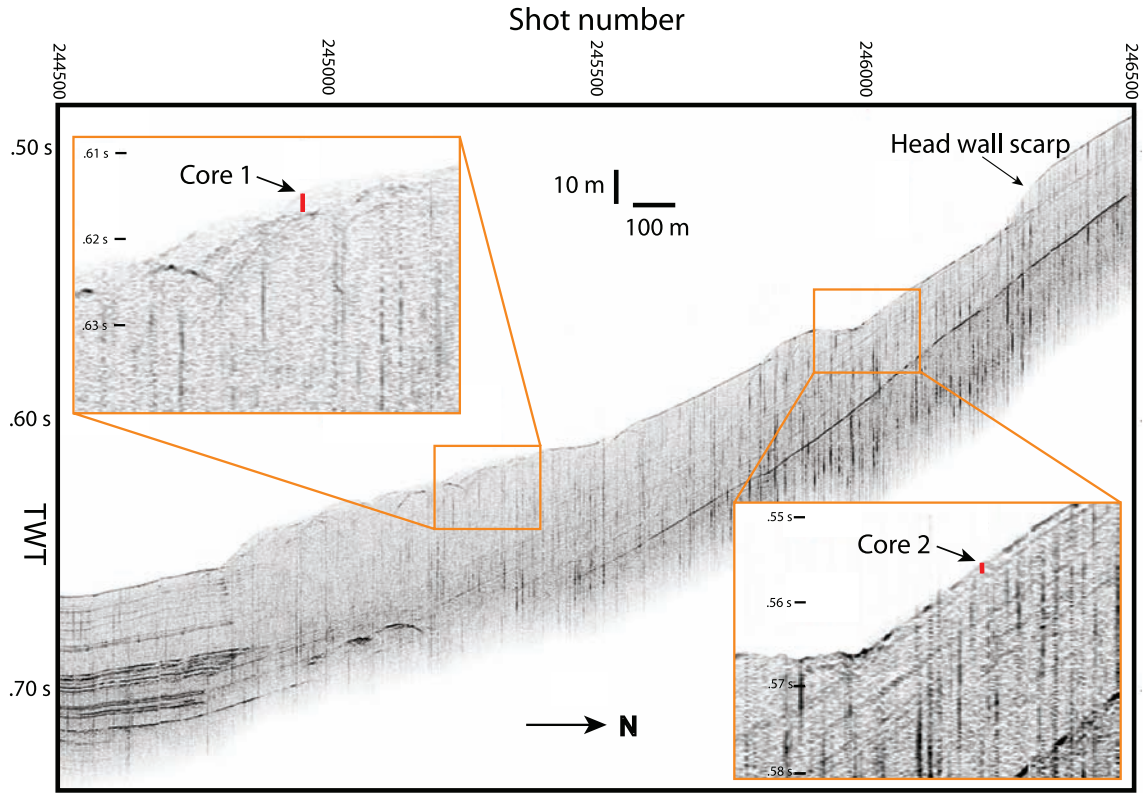

Figure 4. CHIRP seismic line imaging the western half of the Gaviota Slide. Line extends 2.5 km from 509 mbsl (120°06′30.00″W, 34°21′09.00″N) upslope to 377 mbsl (120°06′29.00″W, 34°22′31.00″N; line a in Figure 3). Cores 1 and 2 are marked in red in the figure insets with length scaled to a velocity of 1500 m/s. The vertical axis is two-way travel time (TWT) in seconds. The horizontal axis is in shot numbers, and the scale bar is based on the average number of shots per 100 m. Note that the CHIRP firing rate varies with water depth. Core 1 is located in the accumulation zone of the Gaviota Slide in an area of disrupted reflectors. Core 2 was collected in the evacuation zone of the slide and penetrates the overlying drape into the material below the slide surface.

at a slope of 0.6°. The material was able to fail at a slope of just 1°, that may be very similar to the low-angle slide that *Field et al.* [1982] describe near the Klamath River, CA. It is possible that there was a wide spread underconsolidation zone or clay-rich layer that allowed for easier mechanical failure during an earthquake event.

4.4. Crack

[28] A large crack (Figure 3) is evidence of recent deformation on the northern side of the basin. This crack extends 8 km, trending east-west between the Goleta and Gaviota slides from 120°00′17.55″W, 34°22′28.92″N at a depth of 355 meters on the east to 394 meters on the west at 120°05′34.75″W, 34°22′22.67″N. The slope across the crack ranges from 4.9° to 5.5°. The crack continues from the western edge of the Gaviota Slide another 2.4 km before dying out where the slope diminishes to 3.9°. The crack is less defined along its eastern extent and is overprinted by larger rills that exhibit up to 5 meters of relief. These rill features appear similar to those described by *Spinelli and Field* [2001] north of the Humboldt amphitheater in northern California.

5. Methods and Results

5.1. CHIRP Seismic Data

[29] Seismic lines covering the northern slope of the SBB were collected during August 2004 using the Scripps Institution of Oceanography subbottom unit (Figures 4 and 5). The CHIRP seismic system [*Schock et al.*, 1989] is a modified EdgeTech Xstar system with an ADSL link from the fish to the topside computers. The data were collected with a 50 ms sweep from 1 to 6 kHz. The Xstar SEG-Y records were processed with seismic-py and SIOSEIS (P. Henkart, SIOSIES, http://sioseis.ucsd.edu,

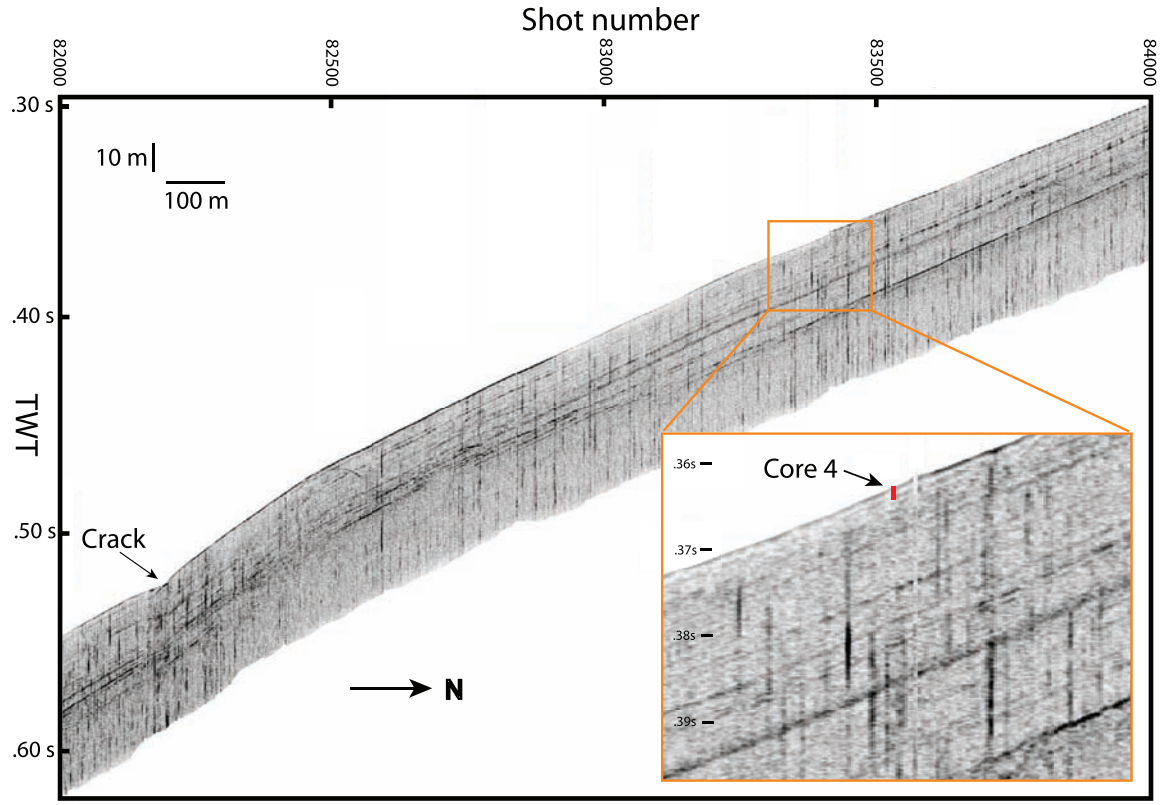

Figure 5. CHIRP seismic line across the crack between the Gaviota and Goleta slides. This line extends 1.9 km from 420 mbsl (120°03′30.00″W, 34°22′09.00″N) upslope to 247 mbsl (120°03′20.00″W, 34°23′09.00″N; line b in Figure 3). Core 4 is marked in red in the figure inset with length scaled to a velocity of 1500 m/s. (See also caption in Figure 4.)

2005), and were plotted with pltsegy. (The seismic-py software is available from the authors upon request.)

5.2. Coring

[30] Cores were acquired with the Scripps Institution of Oceanography "King Kong" gravity coring device using clear plastic core liner with an inner diameter of 8.26 cm. The core head was loaded with 136 kg and deployed at 30 m/minute into the sea floor. Table 1 summarizes the three cores collected for this study and the nearby ODP Site 893 (see Figure 2).

[31] Biogenic gas could potentially disturb the fabric of the cores as they are brought up from depth. By using clear core liner, we were able to observe the sediment-water interface and overlying water clarity as soon as it was removed from the core barrel. On deck, we observed excellent preservation of the sediment-water interface complete with hummocky bioturbated sediments. We observed no evidence of deformation as a result of gas expulsion.

[32] All cores were split, described, photographed, and X-rayed. Cores were then sampled with 8 cm^3 paleomagnetic cubes as densely as practical with a typical spacing of 3 cm. The 8 cm^3 specimens were weighed wet, dried by cooking at 50° C, and then weighed dry to determine weight percent water.

[33] Core 1 (Figures 4 and 6) was collected from the accumulation zone of the Gaviota Slide at a water depth of 480 meters. The sediment was initially deposited in the oxygenated zone where bioturbators could potentially disturb depositional layering. The sediment was then transported by slope failure to the top of the low-oxygen zone. The top 20 cm of the core was disturbed (photo Figure 6) during transport and splitting. The feature at 40 cm is a section boundary. The rest of the core shows faint sediment layers with some mottling. The core is a dark gray color (Munsell 5Y/3/2).

[34] Core 2 (Figures 4 and 7) was acquired in the evacuation zone of the Gaviota Slide. There is a

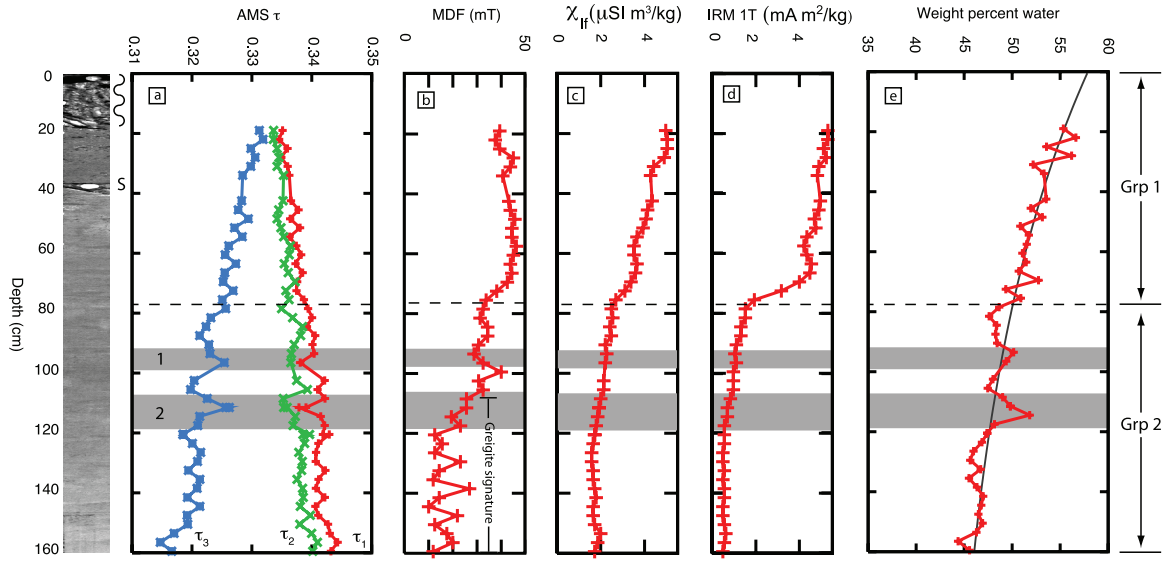

Figure 6. Core 1 is located in the toe of the Gaviota Slide (Figures 3 and 4). On the left is the core photograph. To the right of the core photograph are the major core features. The top 20 cm of the core is disturbed (wavy region), and the discontinuity at 40 cm is a section boundary (S). (a) AMS eigenvalues. τ_1 is the maximum eigenvector, while τ_3 is the minimum, and $\tau_1 + \tau_2 + \tau_3 = 1$. The core has a general trend down core of increasing anisotropy with a more oblate fabric. (b) Median destructive field (MDF). (c) Bulk susceptibility (χ_{lf}) shows a gradual decrease down through the core. (d) Isothermal remanent magnetization (IRM) shows an abrupt transition at the dashed line. Greigite like behavior is marked for the bottom region of the core. (e) Exponential fit to water content data. Core 1 has two zones of high water content that are marked as 1 and 2. These zones correlate to areas of lower anisotropy. The weight percent water is calculated by dividing the weight of 8 cm^3 of dried material from the wet weight. On the right are indicated the extent of groups 1 and 2. Group 1 has high MDF, χ_{lf}, and IRM. Group 2 has low MDF, χ_{lf}, and IRM.

very thin disturbed zone at the core top (<7 cm) and a thin zone at 10 cm where the core was disturbed during splitting. There is a wavy surface at ~27 cm that we interpret to be an unconformity separating the sediments exhumed by the slide below from the more recent pelagic drape above. The preslide layer may be capped by a thin veneer of slide rubble. On the basis of the height of the head wall (Figure 4), it appears that the material below the slide scar had been buried to a depth of 6 to 10 meters before being exhumed. Below this unconformity, the sediment exhibits a marked increase in induration. Occasional burrows are observed, but the core is generally a monotonous gray sediment.

[35] Core 4 (Figures 5 and 8) was collected above the crack to assess if deformation was occurring upslope. This 125 cm core is generally homogeneous in texture and color (dark gray). Slight core splitting disturbance is observed down to ~13 cm. The top 35 cm of sediments have a water-saturated, dark appearance and the bottom 25 cm have a slightly lighter color. There are a few zones that exhibit laminations (40–50 cm, 58 cm, 80–82 cm) and from 15 to 25 cm there are well-preserved burrows (Figure 8). There are a few shells and shell fragments in the 18–22 cm interval and at 62 cm. This core was acquired in an area with continuous seismic reflectors that suggest little to no evidence for internal deformation (Figure 5).

5.3. Remanence Measurements

[36] Magnetic remanence measurements were performed at the Scripps Paleomagnetic Laboratory using 3-axis CTF and 2-G cryogenic magnetometers. Alternating Field (AF) demagnetization was accomplished using a Sapphire Instruments SI-4 in steps up to 40–180 mT depending on the particular specimen's demagnetization curve. Specimens were demagnetized along all three axes with Z being last. Double or triple demagnetizations were not used. Representative Zijderveld diagrams are shown in Figure 9.

[37] There are two styles of demagnetization behavior. The first (Figure 9: Core 4 - 012 cm) is characterized by smooth decay to the origin with median destructive fields (MDF) of around 30 mT. The second is characterized by low MDF values

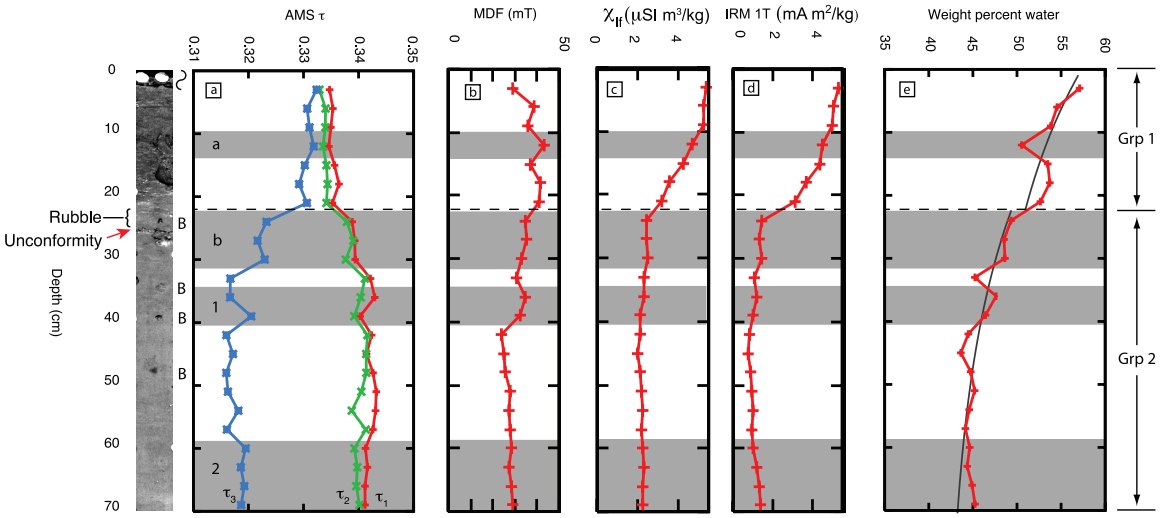

Figure 7. Core 2 is located in the evacuation zone of the Gaviota Slide (Figures 3 and 4). Features are denoted on the right of the core photo. B's are the locations of burrows. There is a zone of disturbed material 7 cm from splitting. The red arrow marks the unconformity on the core photograph. (a) The AMS eigenvectors show a strong jump to a more anisotropic fabric for the specimens at 24, 27, and 30 cm below the sediment water interface. Below 33 cm in the core, the AMS signature is more constant. (b) MDF. (c) χ_{lf}. (d) IRM. (e) Exponential fit to water content data. The fit is not robust because of the low number of data points and the presence of a large unconformity. The weight percent water shows a transition to a constant value at 42 cm depth. Zone a is soft material which was damaged by the coring process. The dashed line shows the Group 1 to Group 2 transition.

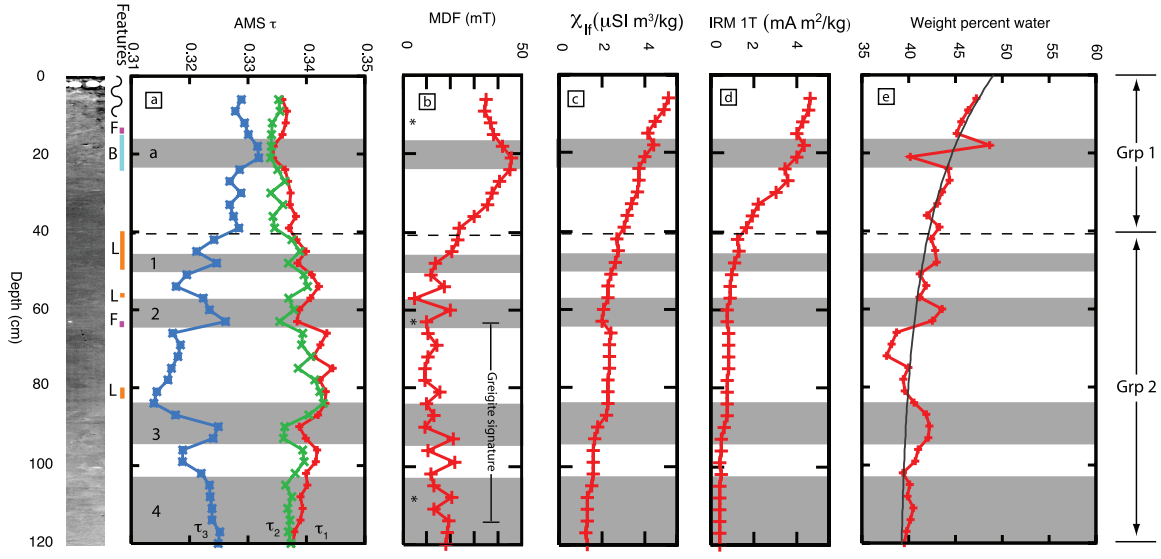

Figure 8. Core 4 is located above the crack between the Gaviota and Goleta slides (See Figures 3 and 5). On the left, important core features are marked: shell fragments in magenta, burrows in cyan, and layering in orange. Zone a is caused by burrows that were identified in an x-radiograph. The dashed line shows the IRM transition. (a) Anisotropy shows a systematic trend increasing down to 84 cm. Zones 1, 2, and 3 deviate from this trend of compaction. (b) The median destructive field reaches a constant baseline by 48 cm depth. Vector end point diagrams for three AF demagnetizations (located by asterisks (*)) are shown in Figure 9. (c) χ_{lf}. (d) IRM. (e) The exponential fit to the water content data shows increased water content for the three gray zones. Between layers 2 and 3 is a zone of lower water content (down to 38%). The exponential fit was only applied down to 84 cm because of the size of zones 2 and 3.

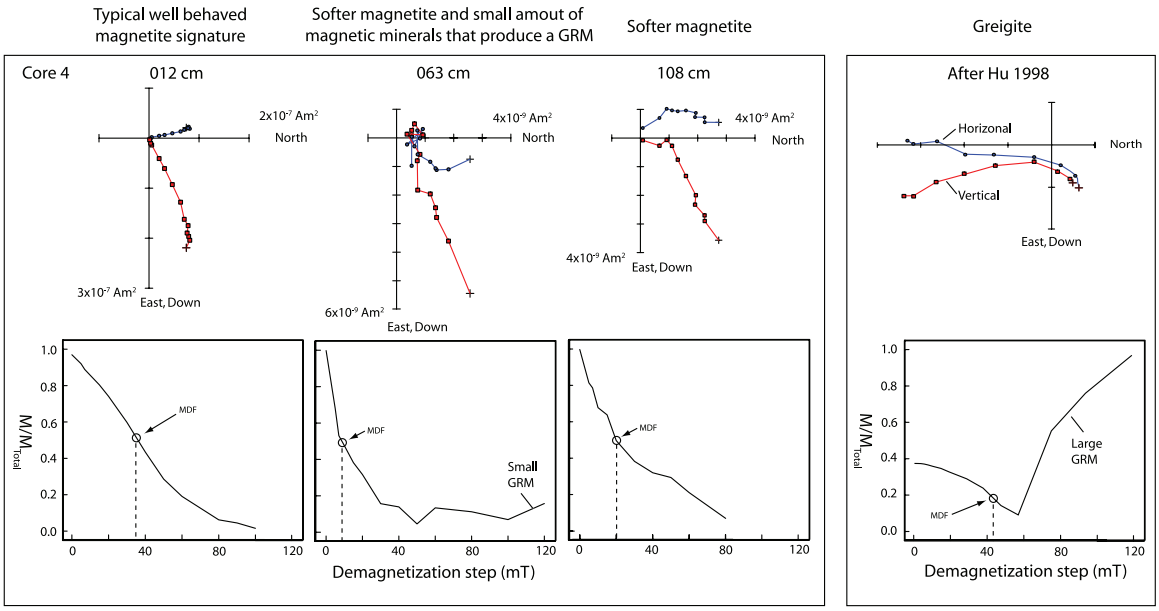

Figure 9. Zijderveld plots showing examples AF demagnetization data. Horizontal projection, blue circles, and vertical component (north-down), red squares, are shown in the top of the figure. The greigite sample [*Hu et al.*, 1998] exhibits demagnetization vectors that diverges away from the origin as it acquired a gyroremanent magnetization (GRM). The bottom plot shows that the intensity increases for demagnatizations above 60 mT. The locations of these samples from core 4 are shown in Figure 8b.

(~10 mT) and a tendency to deviate from the origin, behavior often associated with greigite (Fe_3S_4 [*Snowball*, 1997; *Hu et al.*, 1998]; Figure 9: Core 4 - 063 and 108 cm). The "greigite" signal is characterized by a gyroremanent magnetization (GRM) which is defined as the magnetization acquired during AF that is perpendicular to the applied AF field [*Stephenson*, 1993].

[38] We plot MDF values for the cores in Figures 6–8 in column b. Also shown in Figure 6 and 8 are regions with the "greigite"-like behavior. Core 2 (Figure 7) has no "greigite" signal in the AF demagnetization curves. For comparison, an example of AF demagnetization of a greigite sample (identified with X-ray defraction [*Hu et al.*, 1998]) is shown in Figure 9: Greigite.

[39] Principle component analysis (PCA) was applied to the set of AF demagnetization vectors for each specimen to generate best fit directions [*Kirschvink*, 1980]. *Fisher* [1953] statistics were used to calculate an overall best fit declination for each core. These directions were used to orient all cores ($\bar{D}$, Table 2).

5.4. AMS

[40] Specimens were measured on a Kappabridge KLY-2 magnetic susceptometer, using the 15 position scheme of *Jelinek* [1978]. Eigenparameters

Table 2. *Fisher* [1953] Statistics of Alternative Field Demagnetization of the Natural Remanent Magnetization by Core Sections[a]

Core	Section	$\bar{D}$	$\bar{I}$	N	R	κ	α_{95}	Depth, m
1	1	134.3	50.4	6	5.8591	35	11.4	0.00–0.37
1	2	343.4	45.5	40	34.7466	7	8.9	0.37–1.68
2	1	344.7	56.0	23	20.7940	9	10.1	0.00–0.73
4	1	62.4	52.5	39	36.0973	13	6.6	0.00–1.25

[a] AF, alternative field; NRM; natural remanent magnetization. The declination is in the core section local frame before reorientation to geographic north. On the basis of a Geocentric Axial Dipole (GAD) model, the expected inclination for these cores is 53.8°. Note: $\bar{D}$ is mean declination; $\bar{I}$ is mean inclination; N is number of specimens; R is the length of resultant vector; κ is the *Fisher* [1953] precision parameter; and α_{95} is the estimate of the circle of 95% confidence.

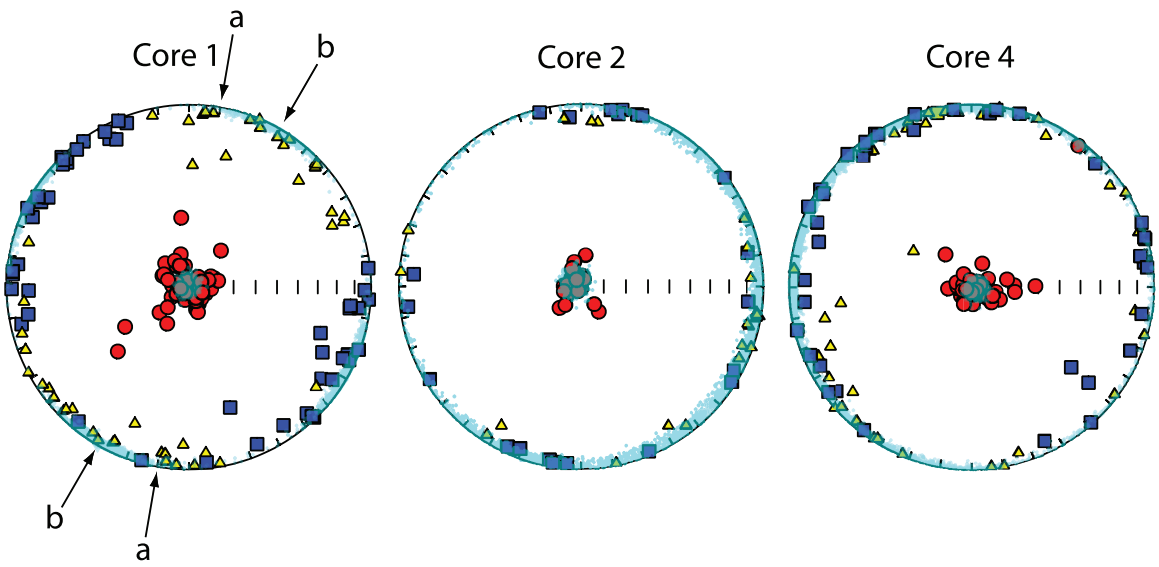

Figure 10. Best fit eigenvectors with the minimum eigenvectors (V_3) as red circles, the maximum eigenvectors (V_1) as blue squares, and intermediate eigenvectors (V_2) as yellow triangles. Cores have been rotated to match the best estimate from principle component analysis (PCA) of alternating frequency (AF) demagnetization of the remanent magnetization. Arrow a on Core 1 shows the direction of compression determined from morphology observed in the multibeam data (Figure 3). Arrow b shows the predicted compression direction based on the best fit perpendicular to the V_1 vectors [*Schwehr and Tauxe*, 2003]. Bootstrap eigenvectors enclosing the 95% confidence bounds are shown in cyan. Note the well-defined confidence intervals for the V_1 in core 1. In contrast, cores 2 and 4 show no preferred orientation of the V_1.

were calculated using Hext statistics [*Hext*, 1963] with PMAG-1.7 (software available at http://sorcerer.ucsd.edu/software/) [*Tauxe*, 1998; L. Tauxe, Lectures in Paleomagnetism, http://earthref.org/MAGIC/books/Tauxe/2005/, Magnetics Information Consortium, 2005]. We followed the convention of *Tauxe* [1998] by referring to eigenvalues as $\tau_{1...3}$, with τ_1 being the largest and τ_3 being the smallest, and the associated eigenvectors as V_1-V_3. Eigenvalues are normalized such that they sum to unity.

[41] In all cores, there is a general increase in anisotropy with depth (measured by the difference between τ_1 and τ_3). The overall trends are interrupted by brief intervals (labeled in Figures 6–8) of decreased anisotropy. Some of these zones appear to be related to core processing disturbances, unconformities or other sedimentological features (e.g., burrows and shell zones). These are labeled with letters in Figures 6–8. Others are not clearly sedimentological in origin. These are numbered in Figures 6–8. These numbered features could be compaction disequilibrium. We will return to this topic later.

[42] Eigenvectors for these cores are plotted in Figure 10 after being oriented assuming the average declinations are approximately north. Also shown are the bootstrapped mean eigenvectors [*Constable and Tauxe*, 1990] which show the mean contour enclosing the 95% confidence bounds. All of these cores show vertical V_3 directions (associated with the minimum eigenvalues and plotted as red circles) as expected in sedimentary environments. Cores 2 and 4 show the oblate fabric with no preferred alignment of V_1, typical of quiet water deposition. Core 1 shows a significant alignment of V_1 in the NW-SE direction, suggesting postdepositional compression. The compressional direction predicted from bathymetry (Figure 3) is shown as arrow "a" in Figure 10. The preferred orientation from the AMS data is consistent with the 95% confidence level for compression along the axis (labeled "b" in Figure 10).

5.5. χ_{lf}, ARM, and IRM

[43] To help constrain the origin of the AMS signatures, we measured low field bulk susceptibility (χ_{lf}), ARM, and IRM. ARM acquisition was accomplished with a SI-4 using a 100 mT alternating field and a 40 μT bias field. IRMs were imparted with an ASC impulse magnetizer with a

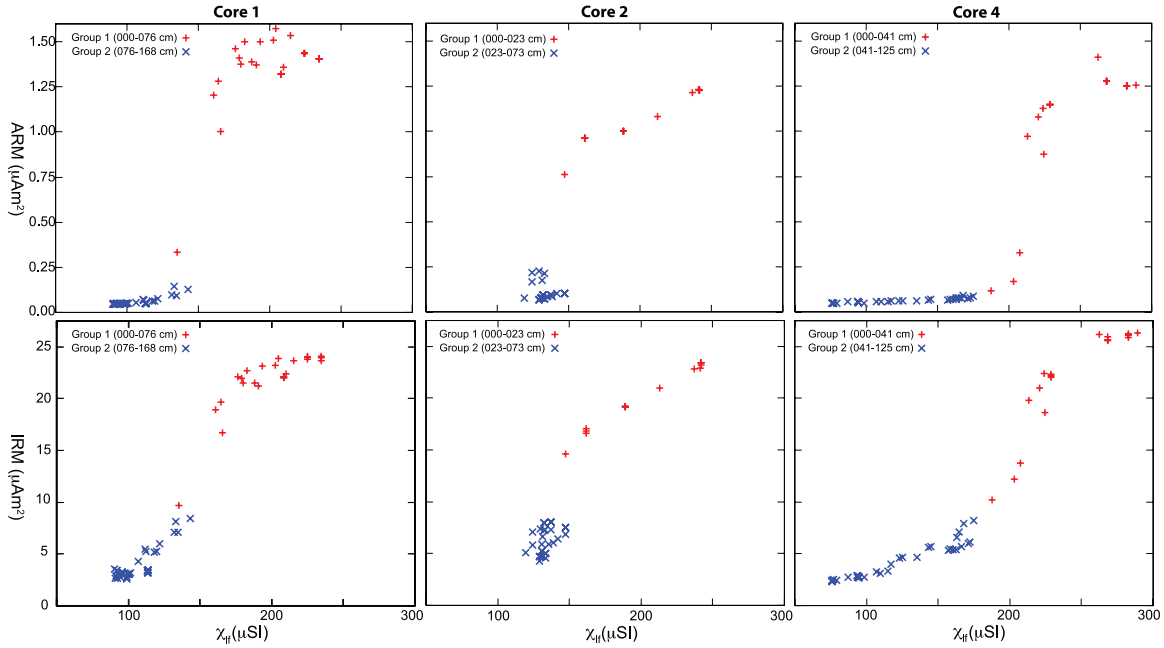

Figure 11. Bi-plots of ARM or IRM versus susceptibility. There are two modal groups of magnetic compositions indicated by pluses and crosses, which are stratigraphically controlled, pluses being core tops.

field of 1 tesla. Mass normalized data used the dry specimen mass after drying at 50°C.

[44] *King et al.* [1983] suggested that different slopes on a bi-plot of χ_{lf} and susceptibility of ARM can show different magnetic grain size fractions. In Figure 11, we plot ARM and IRM against χ_{lf}. These plots show two end members (Group 1 plotted in red pluses and Group 2 as blue stars). According to *King et al.* [1983], the red end member would have smaller grain size compared to the blue end member. Features within either end member are more likely to be caused by fabric, whereas features transitional between the two could well be diagenetic in origin or represent a mixture of the end members.

[45] We plot χ_{lf} and IRM in Figures 6–8, columns c and d, respectively. We have not plotted ARM because it is similar to the IRM behavior. Group 1, with high IRM and χ_{lf} values, is at the tops of all three cores. The transition to Group 2 with lower IRM and χlf is defined by the break in slope after the rapid decrease in IRM (marked with a dashed line in Figures 6–8).

5.6. Hysteresis Parameters

[46] To constrain the magnetic composition of the material in the cores, we measured hysteresis loops for a subset of the specimens (Figure 12) using a

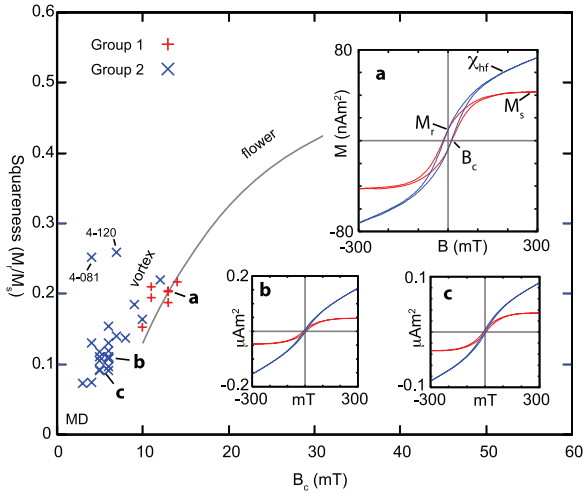

Figure 12. Squareness versus coercive field plot after *Tauxe et al.* [2002]. Insets a–c show representative hysteresis loops for points on the graph. Inset a is enlarged to show the definitions of the hysteresis parameters. The blue loop is the uncorrected measurements of the magnetization (M) induced by an applied field (B). The slope of the blue raw loops where they converge is used to calculate the high field susceptibility (χ_{hf}). The rest of the parameters are calculated from the red slope, which is created by removing the blue high field slope. The bulk coercivity (B_c) is a measure of how stable the magnetic grains are and is the point where the red curve crosses the x axis. M_s is the saturation magnetization. M_r is the saturation remanence where the red loop intersects the y axis as the applied field is lowered from M_s.

Table 3. Specimen Susceptibility Measurements[a]

Core	Depth, m	Figure	$\chi_{lf}\mu$SI	$\chi_{hf}\mu$SI	χ_{hf}/χ_{lf}
1	0.635	12a	182.4	82.7	0.45
2	0.270	12b	133.1	123.1	0.93
3	0.810	12c	162.9	82.0	0.50

[a] A MicroMag 2900 Alternating Gradient Force Magnetometer (AGFM) was used for high field susceptibility (χ_{hf}) and a KLY-2 Kappabridge for low field susceptibility (χ_{lf}) results.

MicroMag alternating gradient force magnetometer (AGFM). The high field susceptibility (χ_{hf}) is dominated by the paramagnetic grains, while the low field bulk susceptibility (χ_{lf}), (derived from the Kappabridge measurements) is a combination of ferro-magnetic and paramagnetic grains. The χ_{hf}/χ_{lf} ratio gives a rough estimate of the fraction of paramagnetic and ferro-magnetic grains contributing to the low field magnetic susceptibility measurements (hence the AMS). The χ_{hf}/χ_{lf} ratios range from 0.45 to 0.93, indicating that the high field, or paramagnetic, contributes a substantial portion of the low field susceptibility (Table 3). The paramagnetic susceptibility is, in turn, largely controlled by the clays. Hence, to a first order, the AMS signal reflects clay fabric in these sediments.

[47] The specimens plot in the ''multidomain'' and ''vortex'' remanent state region of the graph (Figure 12) based on the magnetic simulations of *Tauxe et al.* [2002]. These results predict that the magnetite grains should be about 115–120 nm in width and somewhat elongate. The two specimens labeled 4-081 and 4-120 are from the ''greigite zone'' in core 4, hence cannot be easily interpreted in terms of micromagnetic modeling of magnetite. As expected from the bi-plots, the Group 1 specimens appear to be finer grained than these in Group 2.

[48] From the foregoing, the numbered zones in Figures 6–8 do not appear to be related to changes in composition or to visible disturbance of the cores. It is possible that these zones reflect compaction disequilibria. As hypothesized, such disequilibria would be reflected in the relative water content of the sediment. To investigate further, we measured water content in the cores.

5.7. Water Content

[49] Specimens were weighed after sampling and then dried to calculate an approximate weight percent water. To look for anomalous water content, the weight percent water data were fit with an exponential curve [*Dugan and Flemings*, 2000] using a nonlinear least-squares (NLLS) Marquardt-Levenberg algorithm. Fitting an exponential is not appropriate for core 2 because there is a clear discontinuity at approximately 27 cm and the core length is not long enough to yield the required number of measurements for a stable fit. We split the fit into two sections at the unconformity and a best fit was approximated.

[50] We coregistered the AMS fabric with the deviation from the exponential fit to determine zones of interest. Lettered zones are reserved for regions that we are confident are caused by diagenesis (core 1), coring deformation (core 2), or bioturbation and burrows (core 4). Locations in the core that show both a decrease in anisotropy and an increase in water content have been numbered from 1 to *n* going down core.

6. Discussion

[51] If sediments are homogeneous, they will compact progressively with depth accompanied by a gradual loss of fluid. It is rare for sediment on the continental slope to be completely homogeneous because there are almost always variations in permeabilities, densities, etc. The dominant internal causes of differences arise from changes in lithology, clay fabric, and bioturbation. Processes such as dissolution of grains, precipitation of cements, and grain breaking are unlikely to be important factors when considering young near surface sediments.

[52] In the cores, there are general trends in compaction as reflected by an overall increase in anisotropy down core. The trends are not uniform, but are punctuated by a large transformation associated with the Group 1/2 transition and smaller features associated with visible deformation (lettered zones) and excess water content zones (numbered zones). We will address each of these features in turn in the following section.

6.1. Group 1/2 Transition

[53] The Group 1/2 transition is indicated by a dashed line in Figures 6–8. This horizon corresponds to an increase in the degree of anisotropy (column a) in all cores with Group 2 specimens having higher anisotropy than Group 1 specimens. All of the numbered zones of decreased anisotropy are within Group 2 and do not appear to be associated with changes in magnetic mineralogy.

[54] The transition in core 2 is associated with the largest jump in anisotropy of any core. Moreover, in this core the Group 2 average anisotropy is the highest of any core. Starting at 23 cm below sea

floor, core 2 has a total anisotropy that increases much faster than observed in the other two cores. The transition to a larger total anisotropy occurs from 23 to 33 cm where anisotropy plateaus to a large relatively constant value.

[55] Core 2 was taken from the evacuation zone above the Gaviota Slide (Figure 3). The transition region shows visible evidence of deformation (Figure 7: core photo) with watery, weak material inter-fingering with highly indurated sediments. We interpret this abrupt shift as the transition from young unconsolidated drape, down through a thin veneer of slide rubble overlying the slide surface. The material beneath the slide scar apparently was buried 6–8 meters before the slide occurred. At that depth the consolidation curve had progressed to the point where there is little change with additional loading. Therefore the degree of anisotropy appears essentially constant over short depth intervals.

[56] Our best estimate for the unconformity is at approximately 23 cm. Assuming sediment accumulation rates ranging from 0.8 m/kyr [*Marks et al.*, 1980] to 1.4 m/kyr [*Duncan et al.*, 1971], consistent with rates derived by *Eichhubl et al.* [2002], we estimate the age of the slide to be between 1715 to 1840 CE, which brackets the 1812 Santa Barbara earthquake.

[57] The transitions in cores 1 and 4 are quite different from that observed in core 2. In these cores, the transition between groups 1 and 2 is not associated with a physical discontinuity. Rather, the transition appears to be a diagenetic front.

[58] A large number of studies have found high χ_{lf}, ARM, and IRM in surficial sediments that shift to lower values between 0.2 to 10 m depth from around the world. For example, *Geiss et al.* [2004] and *Pan et al.* [2005] describe such transitions in lacustrine sediments; *Kumar et al.* [2005] in the eastern Arabian Sea; *Tarduno* [1994] and *Rowan and Roberts* [2006] in the Pacific; *Karlin* [1990], *Liu et al.* [2004], and *Riedinger et al.* [2005] on continental margins; and *Leslie et al.* [1990b] focus on the California Borderland in basins just to the south and east of the Santa Barbara Basin. In these studies, χ_{lf}, ARM, and IRM shift together, however, χ_{lf} often does not decay until slightly farther down core.

[59] There are a number of postulated causes for these observed shifts: (1) changes in sediment supply (possibly on glacial time scales), (2) changes in production and destruction of biogenic magnetite, or (3) pore-water chemistry and biogenic activity that consume a fraction of the magnetic grains.

[60] Pore-water chemistry driving the change is the most likely scenario and is the model favored by *Leslie et al.* [1990b]. The process (detailed by *Leslie et al.* [1990a]) is driven by changes from an oxic environment at the sediment-water interface where sediments go to anoxic conditions as they are buried. This process preferentially consumes the smallest magnetite grains, as magnetite is transformed into iron sulfides. *Karlin* [1990] concluded that magnetic mineral diagenesis is likely to occur in rapidly deposited, sulfidic sediments. On the basis of the AF demagnetization curves, we suspect that a minor amount of greigite may have formed in the base of cores 1 and 4, well below the transition from Group 1 to 2 (Figure 9). Therefore we interpret the Group 1/2 transition in cores 1 and 4 to be caused by a loss of fine grained magnetite with small amounts of iron sulfide production occurring deeper down.

[61] The implications for magnetic anisotropy through diagenesis have not been explored in detail in previous studies. Here we find that the finer grained magnetite (Group 1) is likely to be carrying a nearly isotropic fabric. The larger magnetic grains (Group 2) and the paramagnetic minerals carry a fabric that tends to follow the compaction and deformation of the bulk sediment.

6.2. Group 2 Sediments

[62] Below the dashed line in all cores (in the Group 2 layers) are several zones of decreased anisotropy, accompanied by increased water content (labeled as zones 1–4). These zones have a relatively lower anisotropy, and relatively higher water content than the surrounding sediments (as illustrated by Figure 1a in the zone of excess water content). These zones could be caused by either compaction disequilibria, or by mineralogic changes. It appears unlikely in cores 1 and 2 that these are mineralogic changes because neither bi-plots (Figure 11) nor the χ_{lf} and IRM down core (Figures 6 and 7) show major changes in magnetic mineralogy.

[63] The anisotropy and IRM signatures in core 4 show subtle changes associated with zones 1–4. At the base of zone 2, the increase in χ_{lf} and IRM and anisotropy is associated with a shell fragment.

[64] In the regions of low water content, the EF fabric collapses to FF fabric yielding the observed increase in anisotropy. Grain size analysis in core 4 from the top of zone 2 through the area of

increased anisotropy show little to no grain size variability nor a marked change in mineralogical composition. A slight increase in muscovite and biotite in the coarse silt fraction is observed in the region of increased anisotropy between zones 2 and 3, which might account for the subtle increase in χ_{lf} (Figure 8). Detailed examination across this increase in anisotropy using X-ray and visual examination show a minor change in fine scale laminations with an increase of layering at 40–50, 58, and 80–82 cm. This subtle increase in layering might be accompanied by an increase in permeability that limits upward migration of fluids.

[65] Core 1 was acquired within the accumulation zone of the slide, and it is the only core to exhibit a compressional signature in the eigenvectors. The bootstrap mean V_1 trends approximately 30° (shown as arrow b in Figure 10). Despite the compressional signal, core 1 is the most "normal" of all the cores in its compaction signal. The anisotropy shows a general monotonic increase down core as expected from ordinary compaction, punctuated by several excess water content zones. The Group 1/2 transition is the least abrupt in terms of anisotropy of all the cores.

[66] There are several spikes in the water content for core 1 that are observed in the deviation from the exponential fit of weight percent water, two of which coincide with low anisotropy zones. Zone 1 has a decrease in total anisotropy with a minor increase in water content, overlying another short interval of lower water content. Zone 2 is more dramatic than zone 1, with an increase of 7% water content over the general trend. The four specimens in zone 2 also exhibit the strongest decrease in total anisotropy.

[67] In terms of the compaction disequilibrium scenarios outlined in the Introduction, it is possible that zones 1 and 2 are underlying less permeable intervals that act as barriers to fluid migration.

[68] In core 2, as observed in the other cores, the areas of high water content are observed in group 2. Zone b appears to be associated with the unconformity and might record a small layer of slide deposit with small clasts above the unconformity. Zones 1 and 2 appear to be regions of underconsolidation with little to no change in magnetic characteristics as observed in χ_{lf} and IRM.

[69] Core 4 has the most unusual Group 2 of all three cores. From 20 to 50 cm, the anisotropy increases and the water content generally matches the exponential curve. Below this interval of "normal" compaction behavior, there are two main regions that have inverted trends in anisotropy: 57–63 cm and 87–96 cm (zones 1 and 2, respectively). Both of these regions have high water content determined from the weight percent water deviating from the exponential fit. Between these two regions is an area of low water content. Below zone 2, compaction increases slightly and then anisotropy drops again in the excess water zone 3. An increase in anisotropy is observed below zone 3 and might be an impermeable layer preventing upward migration of pore fluid causing excess water content and a slight increase in water down core. Note that the there is little to no corresponding shift of χ_{lf} or IRM at the top of zone 4.

7. Conclusions

[70] The principle results of our rock magnetic and seismic study may be summarized as follows:

[71] 1. AMS, when combined with water content, χ_{lf}, ARM and IRM may add additional information about the compaction history of the sedimentary sequence revealing subtle compaction disequilibria in sediments of relatively uniform composition.

[72] 2. Zones with excess water are associated with less compacted AMS signals (relatively lower anisotropy).

[73] 3. Abrupt change in the degree of anisotropy can reveal unconformities caused by evacuation of slumped material, and exhumation of underlying sediment. These sediments had generally higher anisotropies than equivalent levels in other cores (apparent overconsolidation).

[74] 4. AMS eigenvectors detected the slump with principle strain axis consistent with that expected from the slide morphology.

[75] In summary, anisotropy of magnetic susceptibility is a tool for first order exploration of sediment consolidation state. The approach is able to identify the location of unconformities that have apparent overconsolidation, and can point to horizons that are likely to be underconsolidated. None of the methods for detecting compaction disequilibrium works for every possible situation, but AMS complements the arsenal of techniques used for detecting compaction disequilibria. When looking at AMS signatures, it is important to recognize major lithological changes because a change from clay-rich to sand-rich sediment could be misinterpreted as a major change in sediment compaction, or pore pressure. AMS cannot be used in zones where rapid diagenesis of the magnetic fraction is

occurring. Caution should be used when fitting exponentials to the sediment water content as only small regions of spiking or dipping of water content will be detected.

[76] In addition to underconsolidation, there are other mechanisms for destabilizing sediments on a slope such as zones of weakness associated with certain lithologies or bioturbation, storm wave loading, bubble-phase gas, and oversteepening. Enhancing our understanding of where underconsolidated zones are likely to occur in near surface sediments is helpful for evaluating risk factors associated with slope failure. Excess water content does not necessarily result in slope failure, but it does reduce the normal force of the overlying sediment thus allowing the ratio of shear stress to normal stress to increase. These zones of weakness may be nucleation sites for failures.

Acknowledgments

[77] We would like to thank NSF (grant OCE-04-25919), ONR (grant N00014-03-1-0272), and BP for funding this research. We would also like to thank the crew of the R/V Sproul, the SIO Geological Collections, and the SIO Analytical Facility. Jeff Gee provided invaluable discussion and produced fabulous new software for the magnetometers and Kappabridge.

References

Bennett, R., N. O'Brien, and M. Hulbert (1991), Determinants of clay and shale microfabric signatures: Processes and mechanisms, in *Microstructure of Fine-Grained Sediments: From Mud to Shale*, edited by R. Bennett, N. O'Brien, and M. Hulbert, pp. 5–32, Springer, New York.

Booth, J., D. O'Leary, P. Popenoe, and W. Danforth (1993), U.S. Atlantic continental slope landslides: Their distribution, general attributes, and implications, *Submarine Landslides: Selected Studies in the U.S. Exclusive Economic Zone*, pp. 14–22, U.S. Govt. Print. Off., Washington, D. C.

Borrero, J. C., J. F. Dolan, and C. E. Synolakis (2001), Tsunamis within the Eastern Santa Barbara Channel, *Geophys. Res. Lett.*, *28*(4), 643–646.

Bray, N. A., A. Keyes, and W. M. L. Morawitz (1999), The California Current system in the Southern California Bight and the Santa Barbara Channel, *J. Geophys. Res.*, *104*(C4), 7695–7714.

Constable, C., and L. Tauxe (1990), The bootstrap for magnetic susceptibility tensors, *J. Geophys. Res.*, *95*, 8383–8395.

Dorman, C. E., and C. D. Winant (2000), The structure and variability of the marine atmosphere around the Santa Barbara Channel, *Mon. Weather Rev.*, *128*, 261–282.

Driscoll, N. W., J. K. Weissel, and J. A. Goff (2000), Potential for large-scale submarine slope failure and tsunami generation along the U.S. mid-Atlantic coast, *Geology*, *28*, 407–410.

Dugan, B., and P. Flemings (2000), Overpressure and fluid flow in the New Jersey continental slope: Implications for slope failure and cold seeps, *Science*, *289*, 288–291.

Duncan, J., R. Hoover, C. Pflum, J. Widmier, and C. Daetwyler (1971), Near-surface geology of the Santa Ynez Unit, Santa Barbara Channel, California, Esso Production Research Company Report, pp. 1–58, Houston, Tex.

Edwards, B., H. Lee, and M. Field (1995), Mudflow generated by retrogressive slope failure, Santa Barbara Basin, California continental borderland, *J. Sediment. Res., Sect. A*, *65*, 57–68.

Eichhubl, P., H. G. Greene, and N. Maher (2002), Physiography of an active transpressive margin basin: High-resolution bathymetry of the Santa Barbara basin, Southern California continental borderland, *Mar. Geol.*, *184*, 95–120.

Field, M., J. V. Gardner, A. E. Jennings, and B. Edwards (1982), Earthquake-induced sediment failures on a 0.25-degree slope, Klamath River Delta, California, *Geology*, *10*, 542–546.

Fischer, P. J. (1998), Neogene-Quaternary evolution of the Santa Barbara Basin, California, in *AAPG Pacific Section Meeting*, *AAPG Bull.*, *82*, 846–847.

Fisher, M. A., W. Normark, H. G. Greene, H. J. Lee, and R. Sliter (2005), Geology and tsunamigenic potential of submarine landslides in Santa Barbara Channel, Southern California, *Mar. Geol.*, *224*, 1–22.

Fisher, R. A. (1953), Dispersion on a sphere, *Proc. R. Soc. London, Ser. A*, *217*, 295–305.

Geiss, C. E., S. K. Banerjee, P. Camill, and C. E. Umbanhowar (2004), Sediment-magnetic signature of land-use and drought as recorded in lake sediment from south-central Minnesota, USA, *Quat. Res.*, *62*, 117–125.

Hein, J. R., and J. S. Dowling (2001), Clay mineral content of continental shelf and river sediments, Southern California, *U.S. Geol. Surv. Open File Rep.*, *01-077*, 1–26.

Hendy, I. L., and J. P. Kennett (2000), Dansgaard-Oeschger cycles and the California Current System: Planktonic foraminiferal response to rapid climate change in Santa Barbara Basin, Ocean Drilling Program hole 893A, *Paleoceanography*, *15*(1), 30–42.

Hext, G. R. (1963), The estimation of second-order tensors, with related tests and designs, *Biometrika*, *50*, 353–357.

Hill, J. C., N. W. Driscoll, J. K. Weissel, and J. A. Goff (2004), Large-scale elongated gas blowouts along the U.S. Atlantic margin, *J. Geophys. Res.*, *109*, B09101, doi:10.1029/2004JB002969.

Housen, B., et al. (1996), Strain decoupling across the decollement of the Barbados accretionary prism, *Geology*, *24*, 127–130.

Hu, S., E. Appel, V. Hoffmann, W. W. Schmahl, and S. Wang (1998), Gyromagnetic remanence acquired by greigite (Fe_3S_4) during static three-axis alternating field demagnetization, *Geophys. J. Int.*, *134*, 831–842.

Jelinek, V. (1978), Statistical processing of anisotropy of magnetic susceptibility measured on groups of specimens, *Stud. Geophys. Geod.*, *22*, 50–62.

Karlin, R. (1990), Magnetite diagenesis in marine sediments from the Oregon continental margin, *J. Geophys. Res.*, *95*, 4405–4419.

Kawamura, K., and Y. Ogawa (2004), Progressive change of pelagic clay microstructure during burial process: Examples from piston cores and ODP cores, *Mar. Geol.*, *207*, 131–144.

Kayen, R. E., W. C. Schwab, H. J. Lee, M. E. Torresan, J. R. Hein, P. J. Quinterno, and L. A. Levin (1989), Morphology of sea-floor landslides on Horizon Guyot: Application of

steady-state geotechnical analysis, *Deep Sea Res. Part A*, *36*, 1817–1839.
King, J., S. K. Banerjee, and J. Marvin (1983), A new rock-magnetic approach to selecting sediments for geomagnetic paleointensity studies: Application to paleointensity for the last 4000 years, *J. Geophys. Res.*, *88*, 5911–5921.
Kirschvink, J. L. (1980), The least-squares line and plane and the analysis of paleomagnetic data, *Geophys. J. R. Astron. Soc.*, *62*, 699–718.
Kodama, K. P., and W. Sun (1992), Magnetic anisotropy as a correction for compaction-caused paleomagnetic inclination shallowing, *Geophys. J. Int.*, *111*, 465–469.
Kopf, A., and J. H. Berhman (1997), Fabric evolution and mechanisms of diagenesis in fine-grained sediments from the Kita-Yamato Trough, Japan Sea, *J. Sediment. Res.*, *67*, 590–600.
Kumar, A. A., V. P. Rao, S. K. Patil, P. M. Kessarkar, and M. Thamban (2005), Rock magnetic records of the sediments of the eastern Arabian Sea: Evidence for late Quaternary climatic change, *Mar. Geol.*, *220*, 59–82.
Lambe, T. W., and R. V. Whitman (1969), *Soil Mechanics*, John Wiley, Hoboken, N. J.
Lee, H. J., K. Orzech, J. Locat, and E. Boulanger (2004), Seismic strengthening, a conditioning factor influencing submarine landslide development, in *57th Canadian Geotechnical Conference*, vol. 57, p. 7, Can. Geotech. Soc., Quebec.
Leslie, B. W., D. E. Hammond, W. M. Berelson, and S. P. Lund (1990a), Diagenesis in anoxic sediments from the California continental borderland and its influence on iron, sulfur, and magnetite behavior, *J. Geophys. Res.*, *95*, 4453–4470.
Leslie, B. W., S. P. Lund, and D. E. Hammond (1990b), Rock magnetic evidence for the dissolution and authigenic growth of magnetic minerals within anoxic marine sediments of the California continental borderland, *J. Geophys. Res.*, *95*, 4437–4452.
Liu, J., R. Zhu, A. P. Roberts, S. Li, and J.-H. Chang (2004), High-resolution analysis of early diagenetic effects on magnetic minerals in post-middle-Holocene continental shelf sediments from the Korea Strait, *J. Geophys. Res.*, *109*, B03103, doi:10.1029/2003JB002813.
Locat, J., and H. Lee (2002), Submarine landslides: Advances and challenges, *Can, Geotech, J.*, *39*, 193–212.
Marks, J., A. Marianos, F. Gonzaga, and C. Pflum (1980), Foraminiferal correlation of Quaternary sediments in the Santa Barbara Channel, California, *Spec. Publ. Cushman Found. Foraminiferal Res.*, *19*, 127–133.
Marsaglia, K. M., K. C. Rimkus, and R. J. Behl (1995), Provenance of sand deposited in the Santa Barbara Basin at Site 893 during the last 155,000 years, *Proc. Ocean Drill. Program Sci. Results*, *146*(2), 61–75.
McCabe, C., M. Jackson, and B. B. Ellwood (1985), Magnetic anisotropy in the Trenton Limestone: Results of a new technique, anisotropy of anhysteretic susceptibility, *Geophys. Res. Lett.*, *12*, 333–336.
Mello, U. T., and G. D. Karner (1996), Development of sediment overpressure and its effect on thermal maturation: Application to the Gulf of Mexico Basin, *AAPG Bull.*, *80*, 1367–1396.
Oey, L., C. Winant, E. Dever, W. Johnson, and D.-P. Wang (2004), A model of the near-surface circulation of the Santa Barbara Channel: Comparison with observations and dynamical interpretation, *J. Phys. Oceanogr*, *34*, 23–43.
O'Leary, D., and E. Laine (1996), Proposed criteria for recognizing intrastratal deformation features in marine high resolution seismic reflection profiles, *Geo Mar. Lett.*, *16*, 305–312.
Pan, Y., N. Petersen, A. F. Davila, L. Zhang, M. Winklofer, Q. Liu, M. Hanzlik, and R. Zhu (2005), The detection of bacterial magnetite in recent sediments of Lake Chiemsee (southern Germany), *Earth Planet. Sci. Lett.*, *232*, 109–123.
Reimers, C. E., C. Lange, M. Tabak, and J. Bernhard (1990), Seasonal spillover and varve formation in the Santa Barbara Basin, California, *Limnol. Oceanogr.*, *35*, 1577–1585.
Riedinger, N., K. Pfeifer, S. Kasten, J. F. L. Garmin, C. Vogt, and C. Hensen (2005), Diagenetic alteration of magnetic signals by anaerobic oxidation of methane related to a change in sedimentation rate, *Geochim. Cosmochim. Acta*, *69*, 4117–4126.
Rowan, C. J., and A. P. Roberts (2006), Magnetite dissolution, diachronous greigite formation, and secondary magnetizations from pyrite oxidation: Unravelling complex magnetizations in Neogene marine sediments from New Zealand, *Earth Planet. Sci. Lett.*, *241*, 119–137.
Schlee, J. S., and J. M. Robb (1991), Submarine processes of the middle Atlantic continental rise based on GLORIA imagery, *Geol. Soc. Am. Bull.*, *103*, 1090–1103.
Schock, S. G., L. R. LeBlanc, and L. A. Mayer (1989), Chirp subbottom profiler for quantitative sediment analysis, *Geophysics*, *54*, 445–450.
Schwab, W. C., H. J. Lee, and D. C. Twichell (Eds.) (1993), *Submarine Landslides: Selected Studies in the U.S. Exclusive Economic Zone*, *U.S. Geol. Surv. Bull. 2002*.
Schwehr, K., and L. Tauxe (2003), Characterization of soft-sediment deformation: Detection of cryptoslumps using magnetic methods, *Geology*, *31*, 203–206.
Shaw, J. H., and J. Suppe (1994), Active faulting and growth folding in the eastern Santa Barbara Channel, California, *Geol. Soc. Am. Bull.*, *106*, 607–626.
Snowball, I. F. (1997), Gyroremanent magnetization and the magnetic properties of greigite-bearing clays in southern Sweden, *Geophys. J. Int.*, *129*, 624–636.
Soutar, A., and P. Crill (1977), Sedimentation and climatic patterns in the Santa Barbara Basin during the 19th and 20th centuries, *Geol. Soc. Am. Bull.*, *88*, 1161–1172.
Spinelli, G. A., and M. Field (2001), Evolution of continental slope gullies on the Northern California Margin, *J. Sediment. Res.*, *71*, 237–245.
Stephenson, A. (1993), Three-axis static alternating field demagnetization of rocks and the identification of NRM, gyroremanent magnetization, and anisotropy, *J. Geophys. Res*, *98*, 373–381.
Tarduno, J. A. (1994), Temporal trends of magnetic dissolution in the pelagic realm: Gauging paleoproductivity?, *Earth Planet. Sci. Lett.*, *123*, 39–48.
Tarling, D. H., and F. Hrouda (1993), *The Magnetic Anisotropy of Rocks*, CRC Press, Boca Raton, Fla.
Tauxe, L. (1998), *Paleomagnetic Principles and Practice*, Springer, New York.
Tauxe, L., H. N. Bertram, and C. Seberino (2002), Physical interpretation of hysteresis loops: Micromagnetic modeling of fine particle magnetite, *Geochem. Geophys. Geosyst.*, *3*(10), 1055, doi:10.1029/2001GC000241.
Thunell, R., E. Tappa, and D. Anderson (1995), Sediment fluxes and varve formation in Santa Barbara Basin, offshore California, *Geology*, *23*, 1083–1086.
Ward, S. N. (2001), Landslide tsunami, *J. Geophys. Res.*, *106*, 11,201–11,216.
Warrick, J., L. Washburn, M. Brzezinski, and D. Siegel (2005), Nutrient contributions to the Santa Barbara Channel, California, from the ephemeral Santa Clara River, *Estuarine Coastal Shelf Sci.*, *62*, 559–574.